Supporting Information

Fully Integrated Patch Based on Lamellar Porous Film Assisted GaN Optopairs for Wireless Intelligent Respiratory Monitoring
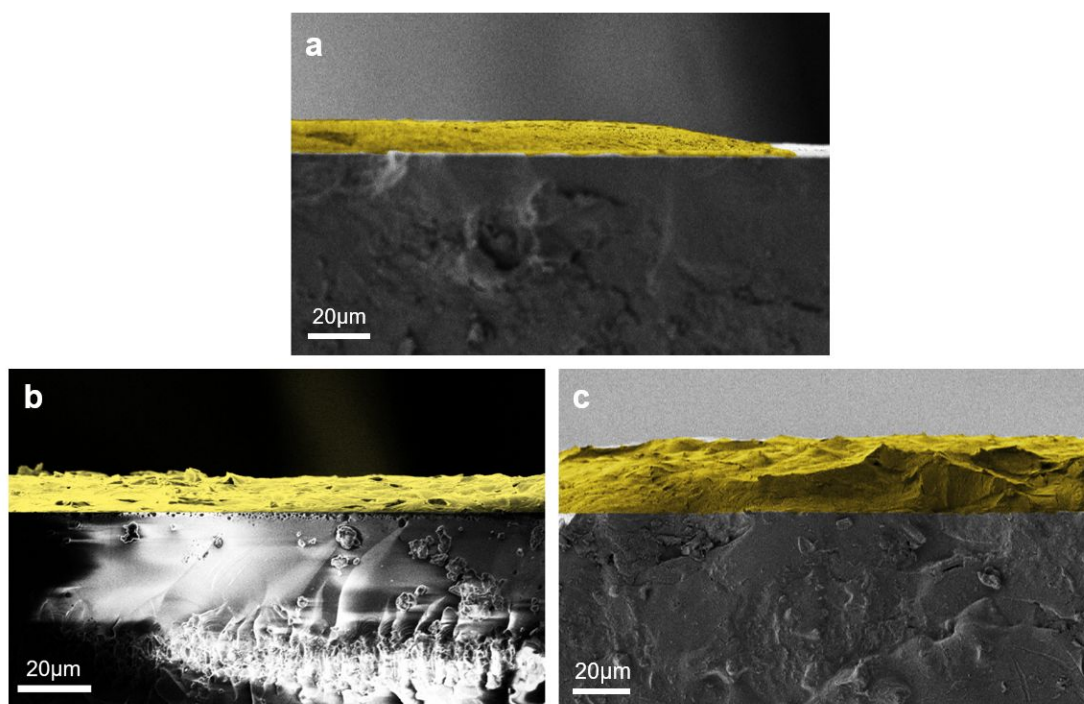
Zecong Liu[#], Junjie Su[#], Kemeng Zhou, Binlu Yu, Yuanjing Lin*, and Kwai Hei Li*

School of Microelectronics, Southern University of Science and Technology, Shenzhen 518055, China

[#]These authors contributed equally to this work.

*Corresponding author. E-mail: khli@sustech.edu.cn, linyj2020@sustech.edu.cn

## S1. SEM images of the cross-section view of the lamellar porous film

Figure S1. False-color SEM images of the cross-section view of the lamellar porous film formed on the GaN device by applying (a) 0.1-µL, (b) 0.3-µL, and (c) 0.5-µL solution drops.

When a small volume of solution drop (e.g. 0.1-µL) is applied, a uniform film cannot

be formed to cover the entire surface of the device, as illustrated in Figure S1a.

Applying 0.3-µL and 0.5-µL solution, the films with thicknesses of approximately 12

µm and 25 µm are obtained, as shown in Figure S1b and S1c.

S2. SEM-EDS test of the lamellar porous film
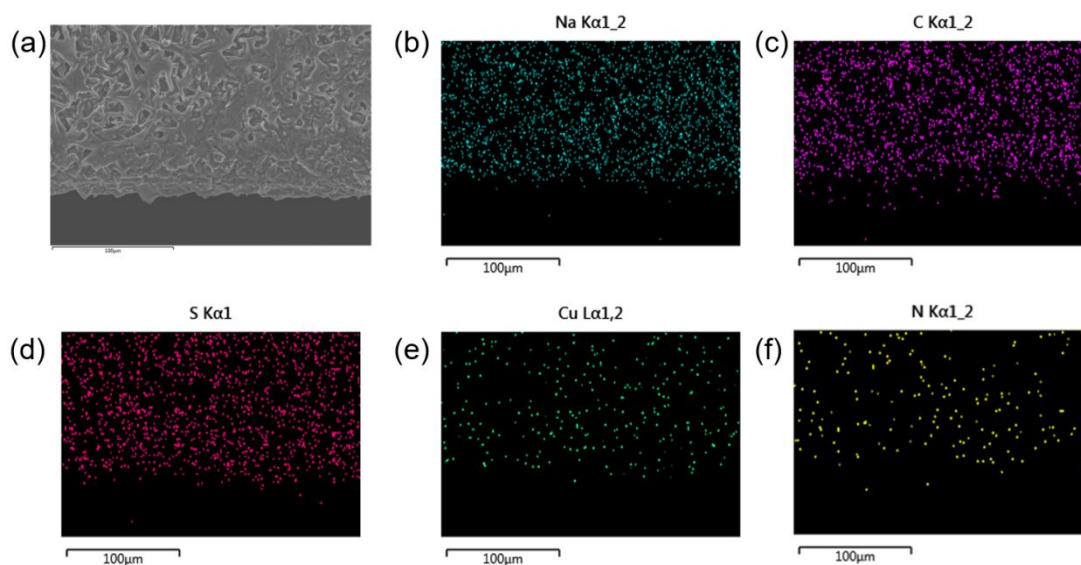
Figure S2. (a) SEM image of the lamellar porous film. (b)-(f) EDS mapping images.

Figure S2 shows the SEM-EDS measurement results of the lamellar porous film. EDS was carried out to explore the elemental composition of the film. The elements C, S, N, and Na were detected in Brilliant Crocein, the dye component of usual red ink. The element Cu was also detected in the complexation of Cu, as inferred by XRD.

S3. Optical properties of the lamellar porous film
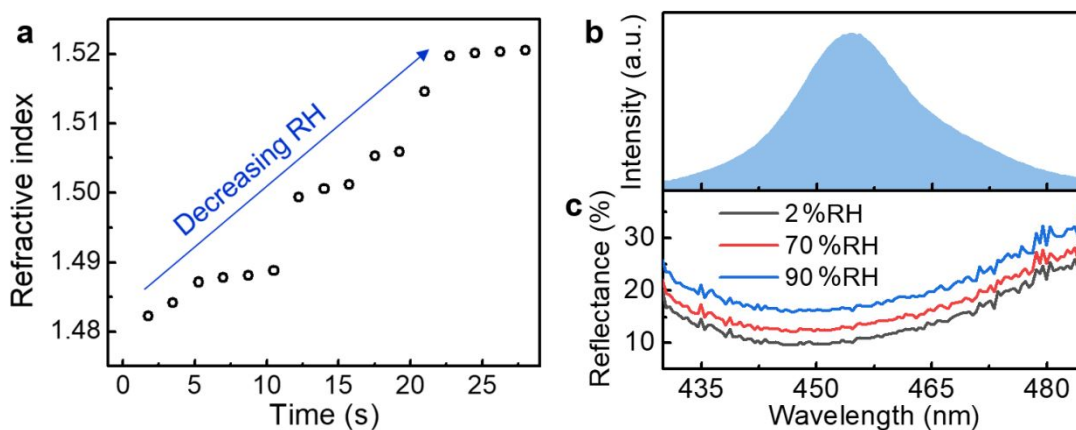
Figure S3. (a) Refractive index of the lamellar porous film measured under conditions of decreasing RH. (b) Emission spectrum of the emitter operating at 10 mA. (c) Reflectance spectra of the lamellar porous film measured at different RHs.

Figure S3a indicates that the refractive index of the porous film increases with decreasing RH, reaching ~1.52, which is the measurement limit of the digital refractometer. Given that sapphire has a refractive index of 1.78, it is expected that the reflectance at the film/sapphire interface decreases with decreasing RH due to the reduced refractive index contrast.

Figure S3b plots the emission spectrum of the GaN MQWs, showing that the emission (wavelength peak = 455 nm, full-width at half maximum (FWHM) = 22 nm) is matched with the variation of reflectance spectra of the film at different RHs, as illustrated Figure S3c. It is observed that the film introduces a more pronounced reflectance change in the range from 70 %RH to 90 % RH than in the range below 70 %RH, suggesting that the response of the film at high RH is higher than at low RH.

S4. Comparison of the humidity-sensing devices sensors

Type	Sensing Materials	Measurement range	Response/ recovery time	Sensitivity	Reference
Capacitive	Metal halide chalcogenide	25-95%	5s	21426 pF/%RH	Advanced Functional Materials, 2020, 30(3): 1907449.
Photoelectric	Chitosan	7.5-83.7%	N/A	N/A	Advanced Optical Materials, 2020, 8(9): 1901932.
Resistive	Two-dimensional mesoporous zinc oxide nanosheets	11.3-97.3%	25s/5s	0.86 ΔR/%RH	Sensors and Actuators B: Chemical, 2019, 293: 83-92.
Optical Fiber	Optical Fiber with Spider silk	32-95%	N/A	11.89 nm/%RH	Sensors and Actuators B: Chemical, 2022, 350: 130895.
Resistive	Paper	41.1-91.5%	472s/19s	N/A	ACS applied materials & interfaces, 2019, 11(24): 21840-21849.
Capacitive	Nano Forest	10-90%	4.7s/5s	N/A	Microsystems & nanoengineering, 2022, 8(1): 1-11.
Resistive	Carbon nano coils	4-95%	1.9s/1.5s	N/A	ACS applied materials & interfaces, 2019, 11(4): 4242-4251.
Capacitive	Laser-induced graphene	10-90%	15.8 s （20-80 %RH）	N/A	Biosensors and Bioelectronics, 2020, 165: 112360.
Capacitive	Hydrogel	4-90%	0.27s/0.3s	N/A	Materials Horizons, 2019, 6(3): 595-603.
Capacitive	MOF	0.71-90%	N/A	0.6 fF/%RH	ACS applied materials & interfaces, 2020, 12(26): 29999-30006.
Capacitive	Keratin	16-92%	21s/56s	633.12 pF/%RH	Sensors and Actuators A: Physical, 2021, 329: 112805.
Resistive	PVA Nano Network	25-98%	148s/110s	0.34 ΔR/%RH	ACS applied materials & interfaces, 2019, 11(47): 44758-44763.
Optoelectronic	GaN device with the lamellar porous film	2-90%	12.5s/6s	13.2 nA/%RH (2%-70%), 61.5 nA/%RH (70%-90%)	This work

**S5. Capability of the device to monitor human breathing patterns**
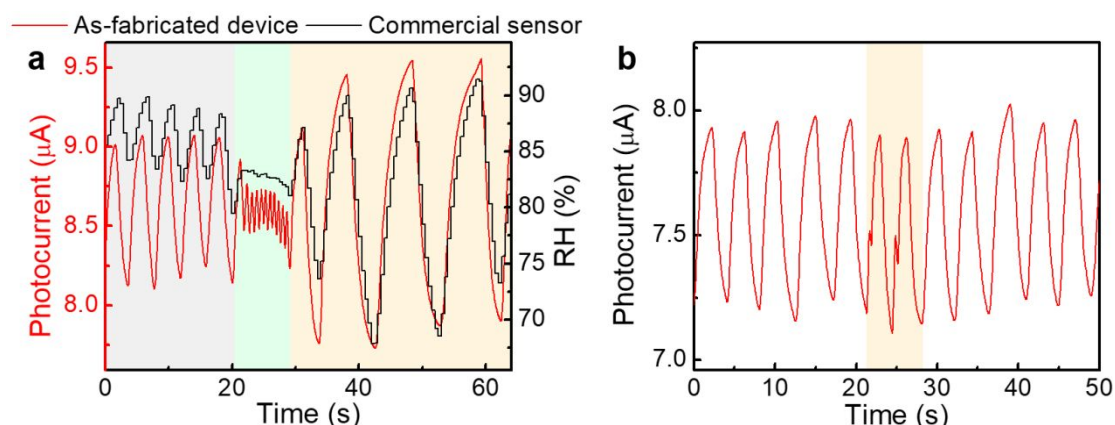
Figure S5. (a) Performance comparison of the as-fabricated device with a commercial device when measuring changes in humidity in a facemask. The blue, green, and orange shaded areas represent normal breathing, fast breathing, and deep breathing, respectively. (b) Photocurrent response of the sensor when monitoring the breathing pattern. The shaded area represents the time period during which the cough occurs.

The as-fabricated device together with a commercial one (SHT3X) operated in an actual human breathing environment inside a facemask. As shown in Figure S5a, the humidity of the breathing inside the mask mainly varies between 70 %RH and 90 %RH. Moreover, it was observed that the as-fabricated device can clearly resolve the periodic patterns under different breathing conditions.

Figure S5b shows another set of realistic experimental observations. When a sudden cough occurred, the device can exhibit distinct profiles different from normal breathing patterns. Such distinguishable patterns will be the key information for the recognition of different breathing modes.

S6. Bending characteristics of the sensing patch
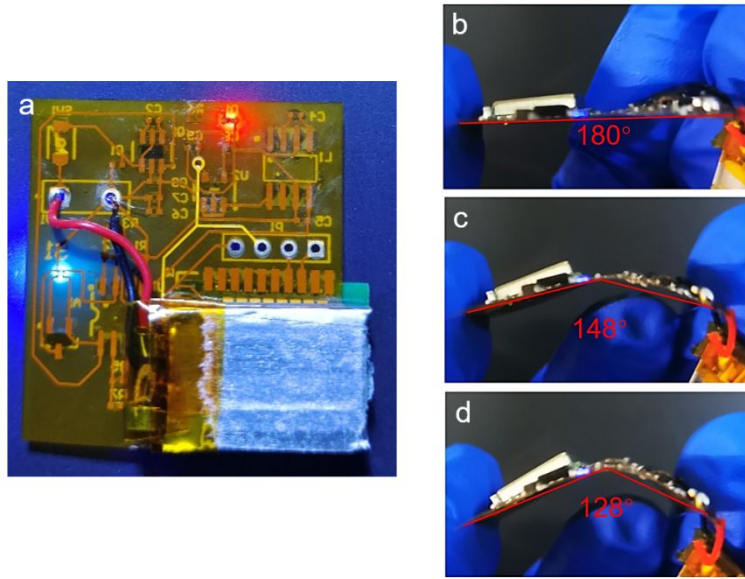
Figure S6. (a) Optical image showing the backside of the PCB with the battery fixed in the bottom left corner. Optical images of the sensing patch bending at different angles of (b) 180°, (c) 148°, and (d) 128°.

A lithium-ion polymer battery (21 mm × 14 mm × 4 mm) with a capacity of 90 mAh at 3.7 V to power the system is molded on the backside of the PCB, as shown in Figure S6a. The battery is intentionally attached to the position behind the Bluetooth Low-Energy (BLE) chip on the PCB, which minimizes its effect on the bending characteristics of the patch. When applying a bend from 180° to 128°, all components on the PCB can work normally without affecting the circuit operation as well as the EL intensity of the GaN device, as shown in Figure S6b-d.

## S7. Results of removing baseline drift and model convergence
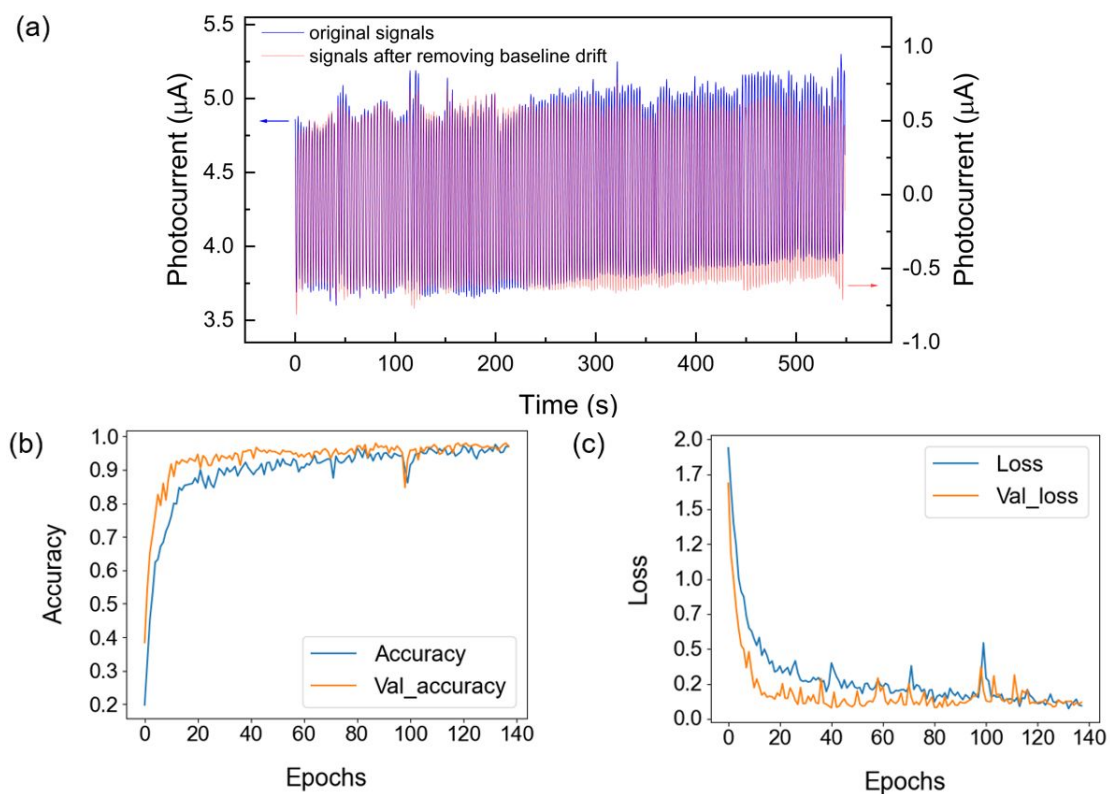
Figure S7. (a) Photocurrent profiles before and after removing baseline drift. (b) Training and validation accuracy versus epochs. (c) Training and validation loss versus epochs.

A Butterworth low-pass filter with a cutoff frequency of 5 Hz was adopted to remove the interference of motion artifacts and variation of environmental RH. Figure S7a shows the signals before and after the subtraction of baseline wander. Figure S7b shows the validation and training accuracy against the number of epochs, and the validation and training loss versus the number of epochs was computed in Figure S7c. As evident from the figures, the model does not overfit and reaches its optimal accuracy at about 120 epochs.

S8. Fabrication procedure of the GaN device
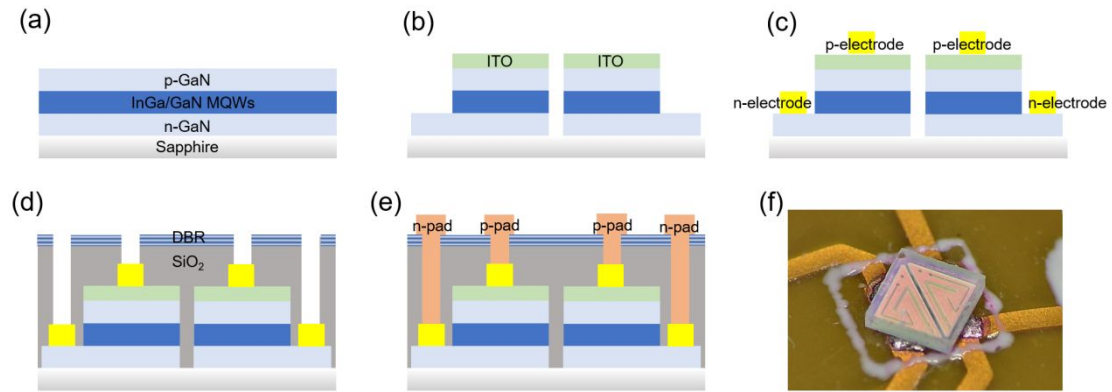
Figure S8. Schematic diagrams of the fabrication process. (a) Growth of GaN epilayer on the sapphire substrate. (b) Mesa etching and ITO coating. (c) Deposition of electrodes. (d) Deposition of SiO$_2$ and DBR. (e) Deposition of metal pads. (f) Micrograph of the packaged device.

The diode optopairs acting as emitters and detectors were formed simultaneously on a GaN-on-sapphire wafer through wafer-scale microfabrication processes, as illustrated in Figure S8a-e. Figure S8f shows a micrograph of the packaged device.

## S9. Deposition of the lamellar porous films on the GaN devices
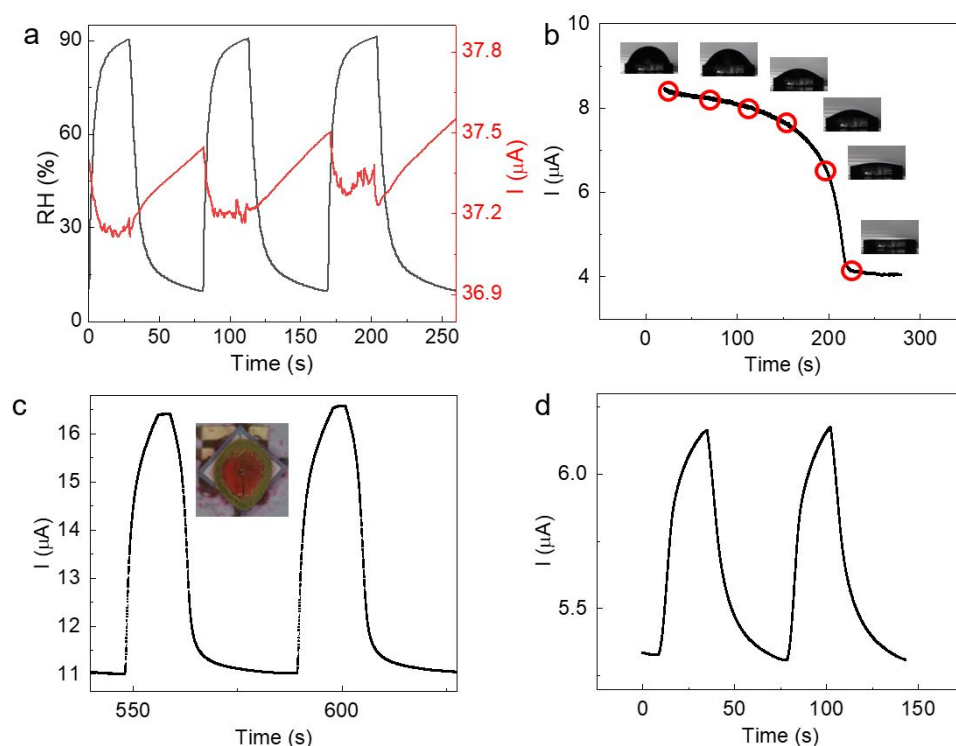
Figure S9. (a) Measured photocurrent response of the bare GaN device to humidity change. (b) Photocurrent variation and droplet morphology of 0.3-µL ink droplets on the sapphire surface of the GaN device during film formation. (c) Photocurrent response (2-90 %RH) and irregular film formation after 0.1-µL ink drops form a film on the device surface. (d) Photocurrent response of 0.5-µL red drops after forming a film on the device surface (2-90 %RH).

Figure S9a plots the photocurrent response of the bare GaN device to humidity change. It is found that the photocurrent change is less than 0.5 µA in the humidity range of 10-90 %RH. The water moisture instantly condenses on the sapphire surface of the device at high humidity, causing a drop of the photocurrent. This unstable ad weak response implies that the bare GaN devices are not suitable for humidity sensing. Figure S9b shows the film formation process of 0.3 µL ink droplet added to the sapphire surface of the GaN chip. The lamellar porous film gradually decreases the photocurrent during the process from the completely wetted state to dry, which is similar to the experimental results. Figure S9c shows the humidity response curve and

the film formation state diagram after 0.1 μL droplet drop is added to the GaN device to form a film. It can be observed that the film does not spread all over the chip surface. The non-uniformity of the film formation also leads to unstable sensing properties of the device. Figure S9d shows the photocurrent response curve of the device after applying a 0.5-μL droplet to form a thick film. The increased thickness of the film increases the response/recovery time to 16 s/19.5 s and reduces the sensitivity. Therefore, a moderate volume of the 0.3-μL droplet is selected during the coating process to achieve the device with balanced sensing performance in terms of stability, sensitivity, and response time.

S10. Design of the wireless data transmission circuit
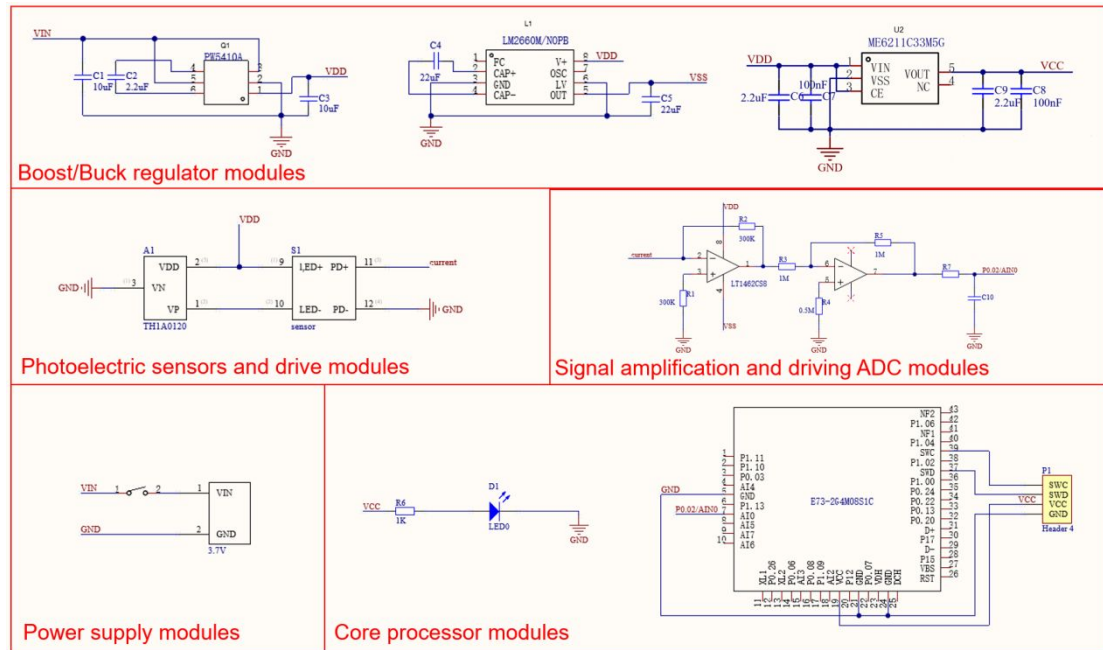
Figure S10. Schematics of the circuit design.

A data transmission circuit is shown in Figure S10. The PW5410A and LM2660M/NOPB regulate the 3.7 V voltage from the lithium-ion polymer battery to ±5 V and supply the signal amplifier module of the LT1462CS8. The ME6211C33M5G-N regulates the 5 V output from the PW5410B to 3.3 V and supplies the signal processing and Bluetooth transmission module of the E73-2G4M08S1C. The TH1A10120 provides a 10-mA constant current source to power the device. The LT1462CS8 amplifies and converts the current signal from the device into a voltage signal and drives the ADC in the E73-2G4M08S1C via RC circuits. The E73-2G4M08S1C is programmed to convert the ADC received signals, then transmit them to other Bluetooth terminal devices.